

Mapping The Neutrino Floor For Dark Matter-Electron Direct Detection Experiments

Jason Wyenberg and Ian M. Shoemaker

Department of Physics, University of South Dakota, Vermillion, SD 57069, USA

(Dated: March 23, 2018)

We study the discovery reach of future Dark Matter (DM) Direct Detection experiments using DM-electron scattering in the presence of the solar neutrino background. At these low energies traditional methods for nuclear and electronic recoil discrimination fail, implying that the neutrino-*nucleus* scattering background can be sizable. We calculate discovery limits based on ionization values of signal and background, and quantify the dependence on the ionization model. Moreover, we explore how the dependence of the DM cross section discovery limits vary with exposure, electronic/nuclear recoil discrimination, DM form factors, and DM astrophysical uncertainties.

I. INTRODUCTION

To date all data on the non-luminous Dark Matter (DM) that dominates the Universe’s matter density is gravitational in nature. Any detection of new DM interactions beyond gravity would represent a critical qualitative advance in our understanding of the most abundant type of matter in the Universe. The Direct Detection method for discovering new DM interactions is afforded by the possibility that DM scattering off some detector material can produce a detectable amount of energy deposition, typically in a deep underground experiment [1]. Traditional detection techniques for \gtrsim GeV DM masses relying on DM-nuclear scattering have made rapid progress [2–11]. Given the relatively weak existing constraints that exist on sub-GeV DM, a number of new ideas for detecting their feeble energy depositions have been proposed [12–19]. Here we focus on the class of experiments that achieve sub-GeV sensitivity by searching for DM-electron scattering [20–25]. To date the DarkSide-50 [26], XENON10 [20], and XENON100 [25] data have set the strongest direct constraints on the DM-electron cross section. Terrestrial stopping effects can be significant for some of the DM models these experiments are sensitive to [24].

DM with sub-GeV masses is not without theoretical motivation as well. In the early Universe, annihilation processes keep the DM in thermal equilibrium until the expansion of the Universe dilutes the DM density enough that annihilation “freezes-out” and the DM abundance becomes fixed in a comoving volume. This is often what is called the WIMP (weakly-interacting massive particle) miracle despite the fact that DM need not be weakly-interacting for this argument to hold. Indeed, as is well-known, a sub-GeV DM candidate interacting only with the weak force would overclose the universe [27]. Instead of the weak force, a conventional benchmark model for light DM interactions is a class of hidden sector models containing a kinetically mixed [28] dark photon [29]. As has been pointed out [21], this class of models can accommodate the observed DM abundance through the thermal relic argument or alternatively via “freeze-in” [30, 31] or asymmetric thermal freeze-out [32, 33], and some of these parameter spaces can be covered by future DM-electron direct detection experiments. Moreover the available mass range for thermal relics has been recently extended to sub-MeV masses [34], which may be testable with DM-

electron direct detection.

As these DM-electron direct detection experiments grow in sensitivity, they will eventually receive irreducible contributions from neutrino fluxes, just as their DM-nuclear counterparts [35–37]. As has been studied, semiconductor-based detectors are particularly promising given their small bandgaps [21]. In this paper we will focus on this class of technologies for DM-electron direct detection.

The motivation to search for electron recoil events can be illustrated as follows. For DM masses $M_\chi \lesssim 1$ GeV, the maximum χ incident energy will be insufficient to produce an observable ionization signal in the detector if the nuclear recoil energy is below the characteristic bandgap energy of the detector. Figure 1 shows how the nuclear recoil observable event rates drop precipitously below a certain value of M_χ for a Ge detector with bandgap energy $E_{gap} = 0.67$ eV. χ -electron scattering may probe the parameter space $M_\chi < 1$ GeV, as the kinematics of a χ -electron scattering event will produce observable recoil energies for incident energies of the χ particle several orders of magnitude smaller than incident energies required to produce observable nuclear recoil scattering events. This superior ability of χ -electron scatter-

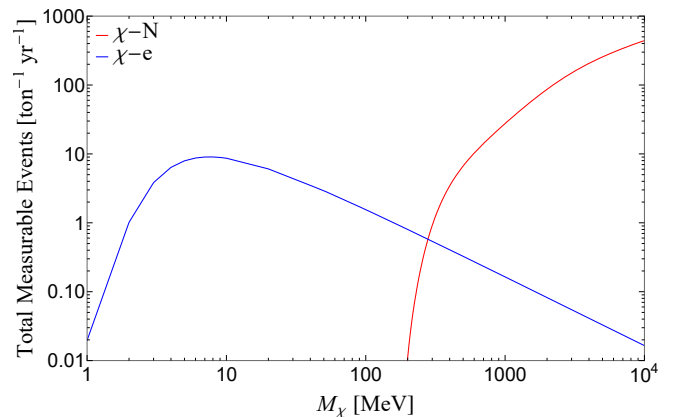


FIG. 1: Total observable event rates of χ -N and χ -e scattering for $\bar{\sigma}_{N,e} = 10^{-44}$ cm² in an ideal Ge detector with the Lindhard ionization model including an adiabatic correction factor as discussed in III D. Note that the event rates for χ -N scattering fall precipitously below ~ 1 GeV, and χ -e scattering produces a significantly higher event rate in the range of ~ 1 to 300 MeV.

ing over χ - N scattering to probe the parameter space $M_\chi < 1$ GeV is apparent from the event rates shown in Figure 1.

The remainder of this paper is organized as follows. In Sec. II we outline the elements of our event rate calculations for both the DM and neutrino contributions. In Sec. III we summarize the assumptions we make for the detector performance. In Sec. IV we characterize the relevant statistical methods we employ for signal discrimination and discovery reach. Sec. V contains our main findings regarding the nature of the neutrino floor at future DM-electron direct detection experiments, including the impact of nuclear/electron recoil discrimination and DM astrophysical uncertainties. Finally in Sec. VI we summarize our conclusions and outline future directions.

II. EVENT RATE CALCULATIONS

A. Signal from χ Scattering

1. Local χ Velocity Distribution

We follow the standard procedure of modeling the χ velocity as a Maxwell-Boltzmann distribution given in [35]:

$$f(\vec{v}) = \begin{cases} \frac{1}{N_{esc}(\pi v_0^2)^{3/2}} e^{-\frac{(\vec{v} + \vec{V}_{lab})^2}{v_0^2}} & \text{if } |\vec{v} + \vec{V}_{lab}| < v_{esc} \\ 0 & \text{if } |\vec{v} + \vec{V}_{lab}| \geq v_{esc} \end{cases} \quad (1)$$

where N_{esc} is a normalization constant, v_0 is the local velocity taken to be 230 km/s, \vec{V}_{lab} is the velocity of the lab (earth) relative to the galactic rest frame taken to be 240 km/s, and v_{esc} is the galactic escape velocity taken to be 600 km/s. The mean inverse velocity η , with a minimum cut-off velocity v_χ^{min} , is given by:

$$\eta(v_\chi^{min}) = \int_{v_\chi^{min}} \frac{f(v)}{v} d^3v, \quad (2)$$

where $v_\chi^{min} = \sqrt{\frac{2E_\chi^{min}}{M_\chi}}$. We employ the analytic formulae for $\eta(v^{min})$ found in Refs. [38–41].

2. χ -Electron Event Rates

We employed a full wavefunction model of χ -electron scattering using the differential cross-section from [42]:

$$\frac{d\langle\sigma_{ion}^i v\rangle}{d\ln E_R} = \frac{\bar{\sigma}_e}{8\mu_{\chi e}^2} \int q dq |f_{ion}^i(k', q)|^2 |F_\chi(q)|^2 \eta(v_\chi^{min}), \quad (3)$$

where $\mu_{\chi e}$ is the electron- χ reduced mass, q is the momentum transfer between χ and electron, and $F_\chi(q)$ is the “dark” form factor. Our fiducial assumption will be that $F_\chi(q) = 1$ (heavy mediators), though we also examine the $F_\chi(q) = 1/q^2$ case at the end of the paper. f_{ion}^i encodes the wavefunction information of the electronic structure of the atom and how likely

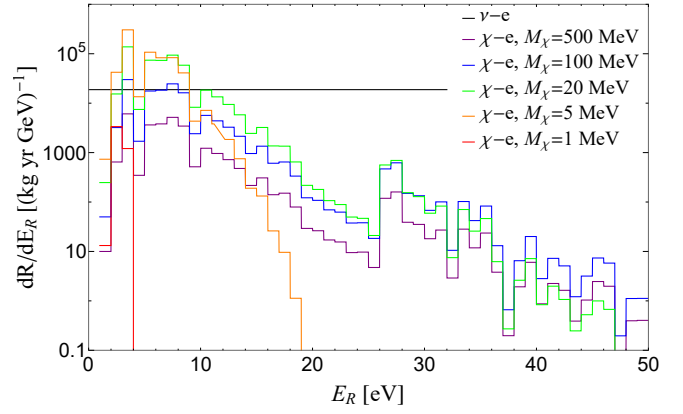


FIG. 2: χ -e signal scattering rates for $\bar{\sigma}_e = 10^{-44} \text{ cm}^2$ and several values of M_χ (coloured curves). Also shown are the ν -e background scattering rates (black curve).

it is that an incoming velocity χ particle will ionize the electron to a given energy. v_χ^{min} is, from simple kinematics,

$$v_\chi^{min} = \sqrt{\frac{2E_\chi^{min}}{M_\chi}}, \quad E_\chi^{min} = E_R \frac{(m_e + M_\chi)^2}{4m_e M_\chi}; \quad (4)$$

The differential scattering rate is given by:

$$\frac{dR}{dE_R} = \frac{n_\chi N_e}{E_R} T \frac{d\langle\sigma_{ion}^i v\rangle}{d\ln E_R}, \quad (5)$$

where $n_\chi = \frac{\rho_\chi}{M_\chi}$ is the number density of the DM particles and $\rho_\chi = 0.4 \text{ GeV/cm}^3$. The number of electrons in the target detector is $N_e = \frac{M_{det}}{M_{Ge}}$, with M_χ , M_{det} and M_{Ge} being the mass of the χ particle, detector and Germanium atom, respectively. We use the results of [21] and the QEdark software package to calculate the differential scattering rate as:

$$\frac{dR}{dE_R} = \frac{\rho_\chi}{M_\chi} \frac{M_{det}}{M_{Ge}} T \frac{\bar{\sigma}_e}{8\mu_{\chi e}^2 E_R} \times \sum_{i=1}^{32} \int q dq |f_{ion}^i(k', q)|^2 |F_\chi(q)|^2 \eta(v_\chi^{min}) \quad (6)$$

The sum over index i is for the number of electrons in the Germanium atom. Figure 2 plots the event rates with 1-eV E_R resolution for several values of M_χ with $F_\chi(q) = 1$, $\bar{\sigma}_e = 10^{-44} \text{ cm}^2$, along with the background ν -electron rates. The event rate profile for χ -electron scattering is distinct from the constant profile of the ν -electron background. For all $M_\chi > \text{MeV}$, the peak event rate is near 6 eV, but for $M_\chi \mathcal{O}(\text{MeV})$, recoil energies are truncated below this peak. The conversion of these event rates to an observable detector signal is discussed in Section III.

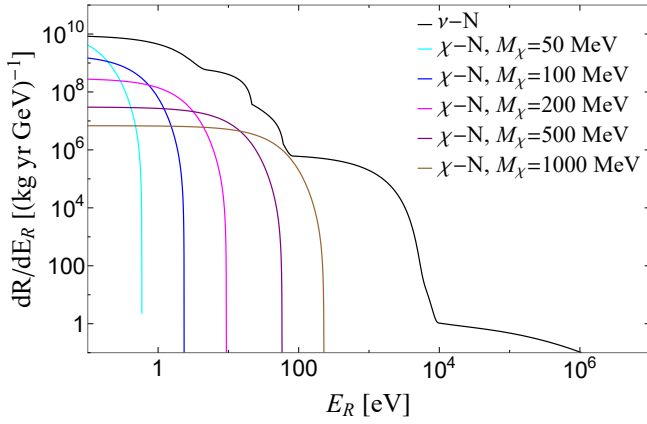


FIG. 3: χ -N signal scattering rates for $\bar{\sigma}_N = 10^{-44} \text{ cm}^2$ and several values of M_χ (coloured curves). Also shown are the ν -N background scattering rates (black curve).

3. χ -Nucleus Event Rates

χ -nucleus scattering was modeled using the differential cross-section from [35]:

$$\frac{dR}{dE_R} = M_{det} T \frac{\rho_\chi \bar{\sigma}_N}{2M_\chi \mu_{\chi N}^2} F^2(E_R) \eta(v_\chi^{min}), \quad (7)$$

where $M_{det} T$ is the experiment exposure, $\bar{\sigma}_N$ is the χ -nucleus cross-section which scales as A^2 times the χ -neutron

$$\frac{d\sigma(E_\nu, E_R)}{dE_R} = \frac{G_f^2 m_e}{2\pi} \left[(g_\nu + g_a)^2 + (g_\nu - g_a)^2 \left(1 - \frac{E_R}{E_\nu}\right)^2 + (g_a^2 - g_\nu^2) \frac{m_e E_R}{E_\nu^2} \right] \quad (8)$$

where m_e is the electron mass, and g_ν and g_a are the vectorial and axial coupling, respectively. Here $g_{a/v,e}$ is taken as $g_{a/v,\tau/\mu} + 1$ due to the additional charged current contribution of the ν_e interaction, where $g_{a/v,e}$ is the axial or vectorial coupling constant for ν_e , and $g_{a/v,\tau/\mu}$ is the same for ν_τ or ν_μ . In this paper, when those solar ν -e backgrounds that are relevant must be considered, the incident energies are low enough that neutrino oscillations can be ignored, and the ν_e fraction is taken to be 0.55. The ν -electron scattering event rate as a function of energy is given by:

$$\frac{dR}{dE_R} = N_e \int_{E_\nu^{min}} \frac{dN_\nu}{dE_\nu} \frac{d\sigma(E_\nu, E_R)}{dE_R} dE_\nu \quad (9)$$

where N_e and N_ν are the number of electrons and neutrinos, respectively, and E_ν^{min} is given by:

$$E_\nu^{min} = \frac{1}{2} \left(E_R + \sqrt{E_R^2 + 2m_e E_R} \right) \quad (10)$$

cross-section, $\mu_{\chi N}$ is the χ -nucleus reduced mass, and F^2 is the nuclear form factor, which we take to be the standard Helm form factor. Figure 3 shows the χ -nuclei scattering rates for several values of M_χ as well as the ν -nuclei background scattering rates. v_χ^{min} is the minimum velocity of the χ particle required to produce a recoil energy E_R . Note that for particular values of M_χ , the event rate profile as a function of recoil energy closely mimics the ν -nucleus background profile.

B. Background from Solar- ν Scattering

1. ν Flux Rates

Figure 4 shows the various ν source flux rates that are irreducible backgrounds to the experiment. For nuclear recoils, all ν types are relevant, but for electronic recoils the pp -chain solar- ν flux provides the dominant background source and other ν sources are irrelevant.

2. ν -Electron Scattering

As discussed in [35], the ν -electron cross section is given by:

To match the form of equation 6, the differential scattering

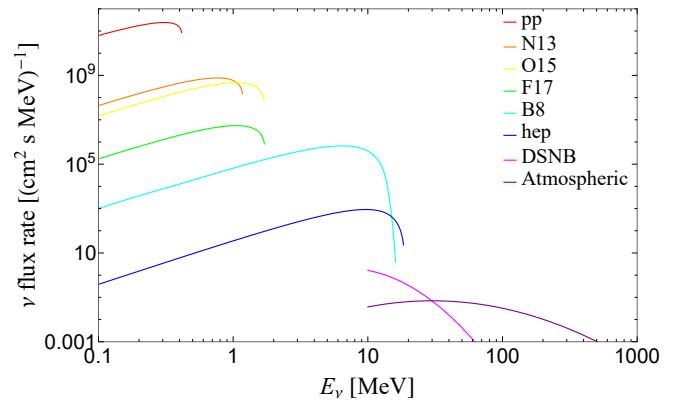


FIG. 4: Solar- ν flux rates from different sources. The dominant background to χ -electron scattering is from the pp -flux.

rate is:

$$\frac{dR}{dE_R} = \frac{M_{det}}{M_{Ge}} T \sum_i \int_{E_{\nu}^{min}} \frac{d\Phi_{\nu}^i}{dE_{\nu}} \frac{d\sigma(E_{\nu}, E_R)}{dE_R} dE_{\nu} \quad (11)$$

where Φ_{ν}^i is the flux of the neutrino source i .

3. ν -Nucleus Scattering

To consider detector experiments which do not have discrimination between electronic and nuclear recoils, we calculate the background ν -nucleus scattering rates. The differential rate is calculated as in equation (9), with m_e replaced by m_N in equation (10), and $d\sigma(E_{\nu}, E_R)$ given by [35]:

$$\frac{d\sigma(E_{\nu}, E_R)}{dE_R} = \frac{G_f^2}{4\pi} Q_w^2 m_N \left(1 - \frac{m_N E_R}{2E_{\nu}^2}\right) F^2(E_R) \quad (12)$$

Here Q_w is the weak nuclear hypercharge with N neutrons, Z protons, and a weak mixing angle θ_w given by:

$$Q_w = N - (1 - 4\sin^2\theta_w)Z \quad (13)$$

Because Q_w is dependent on the number of target neutrons, N , the value of Q_w is modified by the isotope abundance of Ge and Q_w^2 is calculated as:

$$Q_w^2 = \sum_i A_i Q_w^2(N_i) \quad (14)$$

where A_i is the fractional abundance of the Ge isotope with N_i neutrons.

C. Comparison of Nuclear and Electronic Scattering Rates

Putting it all together in Section II, Figure 5 shows event rates for several values of M_{χ} and ν for both nuclear and electron scattering in a Ge detector. Several characteristic features of the electron scattering profiles are superior to that of nuclear scattering for distinguishing sub-GeV χ -e events from backgrounds.

First, for lower values of M_{χ} , the energy threshold for observing nuclear recoil events is several orders of magnitude lower than for electronic recoil events. If the value of M_{χ} lies in the MeV regime, electron scattering could be observed when nuclear scattering is not detectable.

Second, the complicated structure of the Germanium atom electron wavefunction creates a signal profile for electron scattering event rates that is unique from that of the nuclear scattering profile and, more significantly, from the neutrino background rates. This unique profile allows a potential signal to be distinguished from background with greater significance, even when systematic uncertainties dominate at high exposures. For χ -nuclear scattering events,

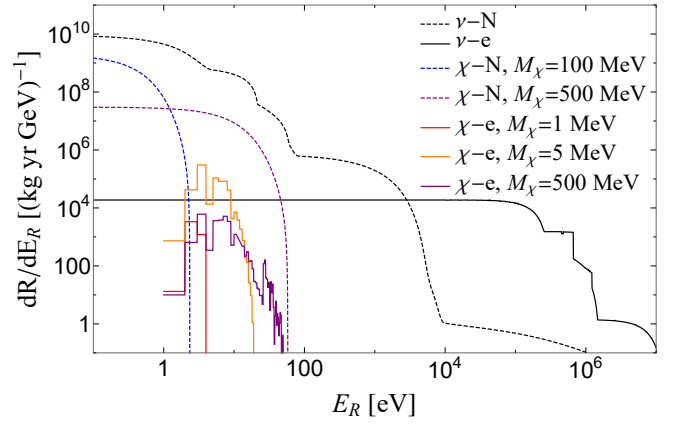


FIG. 5: A comparison of electronic (solid lines) and nuclear (dashed lines) scattering rates. Several values of M_{χ} (coloured curves) for $\bar{\sigma}_{N,e} = 10^{-44} \text{ cm}^2$ are shown along with the ν background scattering rates (black curves). Note that $E_R^{max} < 0.1 \text{ eV}$ for χ -N curves if M_{χ} is below $\sim 50 \text{ MeV}$, while χ -e curves show event rates for M_{χ} as low as $\sim 1 \text{ MeV}$. Note that the observable data is the charge carrier collection as discussed in Section III D and shown in Figure 6. Because of the differing ionization mechanisms following nuclear and electron scattering, the ν -N background to the electron scattering signal is effectively “shifted over” on this plot. The ν -N background rates with scattering recoils of $\sim 50 \text{ eV}$ coincide with the peak signal rates from χ -e scattering recoils of $\sim 6 \text{ eV}$.

the signal profile is featureless and mimics the shape of the neutrino background. For certain values of M_{χ} , the signal profile may match the background neutrino profile closely and the cross-section discovery limit will be high. The χ -electron signal profile never suffers from this impediment.

III. DETECTOR CHARACTERISTICS

To calculate a χ cross-section discovery limit, event rates must be translated into an observable signal based on the detector’s characteristics. The following experimental parameters were modeled:

A. Exposure

The exposure of an experiment, given by its detector fiducial mass and experiment duration (MT), obviously has a great effect on the discovery reach. As noted in [35], for low exposures, background neutrino rates are zero, and the discovery reach scales as $1/MT$. For larger exposures, the discovery reach as a function of exposure enters a regime which scales as $1/\sqrt{MT}$ as the ν background becomes relevant and statistical uncertainties contribute. Finally, for very large exposures where the background ν scattering events are $\mathcal{O}(1000)$, the discovery reach appears more or less constant as a function of exposure due to the systematic uncertainties in the ν flux. In actuality, there is a plateau on the exposure-discovery reach plane, and the discovery reach does slowly

decrease after very great exposures. In theory, and after an infinite exposure, any difference in the signal and background energy profile will elucidate a discovery above the systematic and statistical uncertainties of the ν flux. We explore how the “plateau” evolves with different signal energy profiles in Section V.

B. Energy bin resolution

The size of a detector’s energy bins impacts the ability to distinguish characteristic features of signal and background energy profiles. As the rate profiles in Figure 5 clearly show, the χ -electron scattering rates have a characteristic profile which differs from the background ν scattering rates, a distinction which can be employed to improve the significance of a discovery signal. If a detector cannot “see” the features of this profile, the advantage is lost. For this region of M_χ , we find that bin sizes $\gtrsim 10$ eV “wash out” the characteristic features of the χ -electron scattering energy profile, in which case the likelihood statistical method yields a similar discovery limit “plateau” as the χ^2 test method.

C. Minimum recoil energy threshold

The peak event rates for χ -electron scattering are around $E_R = 6$ eV. The observed event rate of a detector is significantly reduced if the minimum detectable recoil energy is above this threshold, and the discovery reach will be hindered. For M_χ values decreasing below ~ 1 MeV, the max recoil energy of event rates is lowered until $M_\chi = \sim 500$ keV, at which point the max recoil energy of an event is below the 0.67 eV band-gap energy of Germanium and events cannot be seen.

It is possible to lower the band-gap energy by adding dopants to the Germanium crystal as discussed in [43]. Phonons with ionization energies as low as ~ 0.01 eV can ionize or excite impurities and create charge carriers, though the sub-eV recoil energies are small enough that they can be obscured by electronic noise of signal digitization. Charge carriers must be internally amplified in the germanium crystal. With this consideration, it is possible that M_χ values as low as ~ 100 keV could be observed. We do not present results from detectors with dopants in this article and leave this discussion for future work.

D. Recoil energy to ionization conversion

If a χ particle deposits energy onto a Germanium atom, the information collected by the detector will not be the total energy deposited, but rather the ionization signal Q which is a count of the number of electron-hole pairs produced. A simplified treatment of this conversion from energy deposition to ionization signal is employed here. Signal and background

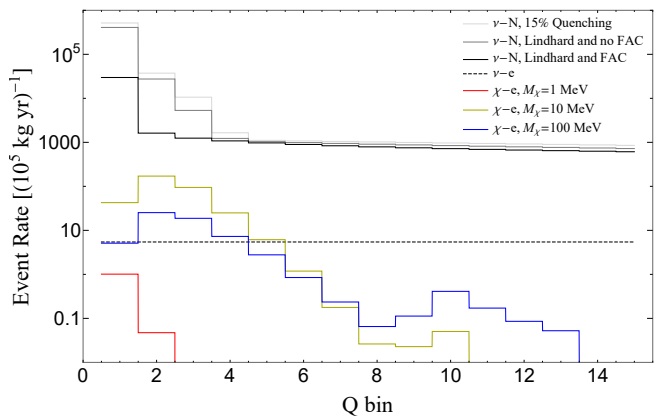


FIG. 6: A comparison of the ν -N observable signals from three models for the nuclear recoil ionization mechanism: 1. 15% quenching (light gray), 2. Lindhard quenching with no adiabatic correction factor (FAC) (grey), and 3. Lindhard quenching with adiabatic correction factor (black). Rates from electron scattering are shown for the ν background (black, dashed) and χ particles (coloured) with $\bar{\sigma}_e = 10^{-44}$ cm².

rate estimates are dependent on the model used for simulating the ionization mechanism after a recoil event.

1. Electron recoils

We follow the method of [21] for the conversion of energy deposited, E_R , to ionization signal, Q , for an electron scattering event:

$$Q_e(E_R) = 1 + \lfloor (E_R - E_{gap})/\varepsilon \rfloor \quad (15)$$

where $\lfloor x \rfloor$ rounds x to the nearest integer. ε and the band-gap energy E_{gap} are taken to be their most optimistic values of:

$$\varepsilon = 2.9 \text{ eV}, \quad E_{gap} = 0.67 \text{ eV} \quad (16)$$

Recoil energies below 0.67 eV are unable to overcome the 1- γ scintillation band-gap energy of a detector, and are undetectable.

2. Nuclear recoils

We follow the method of [44] by using the Lindhard “quenching model” for the conversion of energy deposited, E_R , to ionization signal, Q , for a neutron scattering event:

$$Q_N(E_R) = Q_e(E_R L_Q(E_R)), \quad (17)$$

where

$$L_Q(E_R) = \frac{kg(\varepsilon)}{1 + kg(\varepsilon)}, \quad g(\varepsilon) = 3\varepsilon^{0.15} + 0.7\varepsilon^{0.6} + \varepsilon, \quad \varepsilon = 11.5 Z^{-7/3} E_R/\text{keV} \quad (18)$$

where k describes the energy loss and has a value of 0.1789 for Ge with E_R values below 0.8 keV. We assume the fiducial volume of the detector is large and therefore neglect the losses from charge collection inefficiency, η , in the δ and τ regions near the edge of the detector. We include the adiabatic correction factor:

$$F_{AC}(E_R, \xi) = 1 - \exp[-E_R/\xi] \quad (19)$$

with ξ taken to be 0.16 keV. Figure 6 shows how three models of the ionization mechanism affect the observed event rates of ν backgrounds. Note that the 15% quenching model provides the most conservative estimate of the background signal. The Lindhard model with adiabatic correction factor provides the most optimistic estimate of the background signal, with substantial suppression of the $Q = 2$ bin where the peak event rate of the χ signal occurs.

E. Electronic and Nuclear Discrimination

If a detector has the ability to discriminate between nuclear and electronic recoils, the ν -nucleus scattering rates can be ignored, and the discovery reach of the detector can be lowered by several orders of magnitude. Section V provides a comparison of the discovery limit for a detector with and without discrimination.

IV. STATISTICAL METHODS

A. χ^2 Test Statistics

As a rudimentary check of the χ -electron cross-section discovery limits, we use a simple χ^2 test statistic to indicate a discovery given by:

$$Z_{total} = \sum_i^{N_{bins}} Z_i / \sqrt{N_{bins}}, \quad (20)$$

$$Z_i = \left[2 \left((s_i + \sigma_i^2) \log(1 + s_i/\sigma_i^2) - s_i \right) \right]^{0.5} \quad (21)$$

where s_i is the number of expected signal events in bin i and σ_i is the standard deviation of the background events in bin i

given by:

$$\sigma_i^2 = \sigma_{i,sys}^2 + \sigma_{i,stat}^2, \quad (22)$$

$$\sigma_{i,sys}^2 = \sum_j \left(\Delta\Phi_\nu^j \right)^2, \quad \sigma_{i,stat}^2 = N_i^{events} \quad (23)$$

We then calculate the discovery limit for a given mass M_χ to be the value of σ_χ which yields an expected signal event rate for a value of $Z_{total} = 5$, representing a 5-sigma discovery. In the limit of large exposures, the systematic uncertainty dominates, and Z_i reduces to:

$$Z_i = \frac{s_i}{\sigma_{i,sys}} \quad (24)$$

The “ χ^2 floor” is then calculated by using equation 24 in place of 23. The χ^2 floor is typically close to the discovery limit plateau from the Log-Likelihood Profile method, as discussed in section V B.

B. Likelihood Profiles

The Log-Likelihood Profile method provides a more accurate calculation of the discovery significance from signal and background events. While the χ^2 test statistic method described above allows the event counts in each energy bin, i , to float as independent variables with standard deviations described by $\sigma_{i,sys}$ and $\sigma_{i,stat}$, the Log-Likelihood Profile method does not allow the event count in each energy bin to float separately. Rather, it allows the overall ν -flux uncertainty for each ν source to float and the energy bins event counts all increase or decrease together as dependent variables. Simply put, the χ^2 test statistic method treats each energy bin as a separate experiment, whereas the Log-Likelihood Profile method treats the entire data set of all energy bin event counts as one experiment. In this way, the Log-Likelihood Profile method has a capability to distinguish discrepancies between the signal and background event rate energy profile shapes that the χ^2 test statistic method does not have. The Likelihood Profile is calculated following the method of [35]:

$$\mathcal{L}(\vec{\sigma}_e, \vec{\phi}) = \frac{e^{-(\mu_\chi + \sum_{j=1}^{n_\nu} \mu_\nu^j)}}{N!} \prod_{i=1}^N \left[\mu_\chi f_\chi(E_{r_i}) + \sum_{j=1}^{n_\nu} \mu_\nu^j f_\nu^j(E_{r_i}) \right] \prod_{i=1}^{n_\nu} \mathcal{L}_i(\phi_i)$$

where $\mathcal{L}(\vec{\sigma}_e, \vec{\phi})$ is the likelihood of the observed data (N

event counts with recoil energy values E_{r_i}) occurring as a

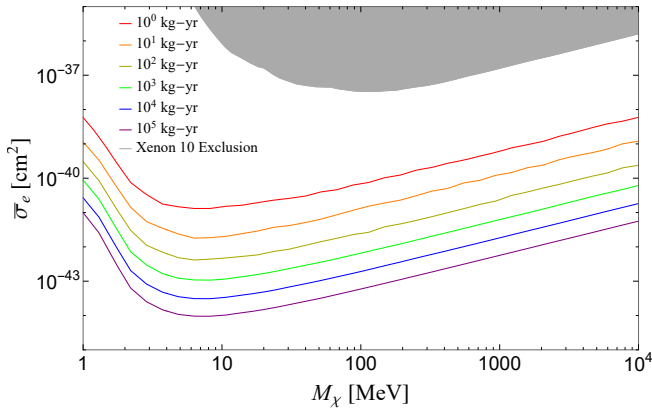


FIG. 7: Discovery limits of a Germanium χ -electron scattering detector for several exposures. The dominant support of the floor is background ν -nucleus scattering. Ionization rates following nuclei scattering events are calculated with a Lindhard quenching model including an adiabatic correction factor. The so-called “soft” and “solid” floors are represented by the yellow and purple curves, respectively. Current exclusion limits from the Xenon-10 experiment shown in [20] are represented by the gray curve.

function of the χ -e cross-section $\bar{\sigma}_e$ and n_ν neutrino source flux rates $\vec{\phi}$. By comparing the likelihood of the observed data assuming no χ signal to the likelihood assuming a hypothesized χ signal, we can calculate a statistical significance of discovery from the data. The ratio:

$$\lambda(0) = \frac{\mathcal{L}(\bar{\sigma}_e = 0, \hat{\vec{\phi}})}{\mathcal{L}(\hat{\bar{\sigma}}_e, \hat{\vec{\phi}})}, \quad (25)$$

where $\hat{\vec{\phi}}$ is the value of $\vec{\phi}$ that maximizes the conditional likelihood ($\bar{\sigma}_e = 0$), and $\hat{\bar{\sigma}}_e, \hat{\vec{\phi}}$ are the values of $\bar{\sigma}_e$ and $\vec{\phi}$ that maximize the unconditional likelihood ($\bar{\sigma}_e$ unbound), profiles over the nuisance parameters of ν -flux uncertainties to present a statistical significance of a χ signal in comparison with the null-hypothesis (background only). $\lambda(0)$ can be used to calculate a test statistic q_0 as:

$$q_0 = -2 \log \lambda(0) \quad (26)$$

Wilk’s theorem states that q_0 follows a χ_1^2 distribution, and the significance of discovery is given by $Z = \sqrt{q_0}$. We calculate the discovery limit for a given mass M_χ to be the value of $\bar{\sigma}_e$ such that the calculated value of Z is equal to 5-sigma for an experiment observing the expectation values of event counts. This is a slight deviation from the method of [35] which defines a discovery limit as the value at which 90% of experiments will achieve a discovery significance of 3-sigma or higher. In our trials, seeking an expected value of 5-sigma yields nearly identical results as seeking a 90% certainty of 3-sigma, with the benefit that calculation speed is increased by several orders of magnitude.

V. FLOOR CALCULATION

A. Discovery Limits

Increasing the exposure of a detector will increase the expected scattering events for a given $\bar{\sigma}_e$ cross-section and hence, lower the value of $\bar{\sigma}_e$ required for an expected event rate. Increasing the exposure of the detector will therefore allow the detector to probe a lower range of the M_χ - $\bar{\sigma}_e$ parameter space. We define the “discovery limit” of the detector as the value of $\bar{\sigma}_e$ that yields an expected discovery significance of 5-sigma for that detector. Figure 7 shows the calculated χ -electron discovery limits as a function of mass for several exposures. Discovery significance is calculated using the Likelihood Profiles method described in section IV B. The ionization of ν -N background scattering events is calculated with the Lindhard quenching model including an adiabatic correction factor.

B. Theoretical Floor

Background event rates will also increase with higher exposures. The term “neutrino floor” is commonly used to describe the lowest cross-section of $\bar{\sigma}_e$ that could be directly detected given that the irreducible background event rates of neutrinos would obscure a potential χ signal for lower values of $\bar{\sigma}_e$. The term “floor” is slightly misleading, because the characteristic energy profile of the $\bar{\sigma}_e$ signal is always distinguishable from the background given large enough exposures, as mentioned in Section III A. There is no “hard floor”. Realistically speaking, however, the exposures required to distinguish the energy profile of the signal from the background are obscenely large, and we can describe an alternative “soft floor” as the point at which the ν event rates become significant, such as when the Log-Likelihood discovery limit as a function of exposure leaves the regime of MT^{-1} and enters the regime of $MT^{-0.5}$. This occurs when the expected ν events are $\mathcal{O}(1)$ in the energy bin with peak χ event rates,

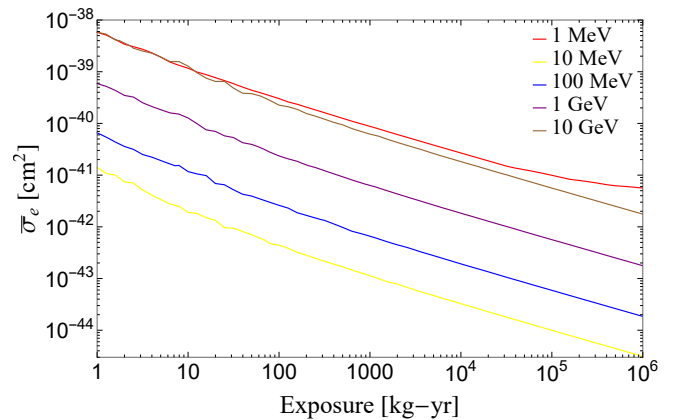


FIG. 8: Discovery limits for several values of M_χ as a function of exposure. The curves transition from a regime of MT^{-1} to $MT^{-0.5}$ around ~ 100 kg yr.

with an exposure $\mathcal{O}(100)$ kg yr. A “hard floor” could be described as the point at which the Log-Likelihood discovery limit enters a “plateau” regime as a function of exposure. However, the exposures necessary to reach this “hard floor” are impractically high. A more practical discovery limit is calculated here. We use the term “solid floor” to be the discovery limit at an exposure of 100 ton yr. The “soft” and “solid” floors are shown by the yellow and purple curves, respectively, in Figure 7.

The discovery limit as a function of exposure is shown in Figure 8 for several values of M_χ . The discovery limit is proportional to the exposure as MT^{-1} for low background events, and transitions to a regime of $MT^{-0.5}$ with increasing background events for exposures above ~ 100 kg yr.

The dominant background is from ν -N scattering. With discrimination between electronic and nuclear recoils, a detector could lower the discovery limit by nearly an order of magnitude, as shown in Figure 9. After the rejection of nuclear recoils, the dominant background from ν -e scattering is several orders of magnitude lower and is dominated by the pp -chain flux.

As noted in [45], the χ signal is modified by uncertainties from several astrophysical parameters. Figure 9 shows how the discovery limit is modified for “optimistic” and “pessimistic” scenarios with ranges of $v_0 = 200 - 280$ km/s, $v_{esc} = 560 - 640$ km/s, and $\rho_\chi = 0.35 - 0.45$ GeV/cm³. We take these two limits of the astrophysical parameters to bracket the range of possible impacts of DM astrophysical uncertainties on the future direct detection discovery limits. This is a conservative estimation in that the further addition of non-Maxwellian features may lead to more extreme deviations in the discovery limits than what we have considered here.

VI. CONCLUSION

The sub-GeV mass range for DM is a well-motivated and under-explored parameter space that may soon be host to much experimental research effort. The discovery reach of future detectors will depend upon their experimental exposure, recoil energy resolution and threshold of detection, and electronic and nuclear discrimination capabilities. A better understanding of the ionization mechanism following a recoil event is needed to fully interpret a potential χ signal. The “soft” and “solid” floors from neutrino backgrounds are provided for χ -electron scattering in comparison with the commonly referenced χ -nucleus floor plot. χ -e scattering events can be detected for χ particles with mass above ~ 1 MeV. χ -N scattering events are detectable only for χ particles with mass above ~ 300 MeV due to the suppression of observable ionized signal rates for smaller masses. We have also shown that astrophysical uncertainties contributing to the χ signal profile modify the potential discovery limit.

This paper could be extended in a number of ways in future work. First, consider some of the ways in which the analysis and experimental techniques could be further developed. As mentioned in Sec. III C, adding dopants to the Germanium

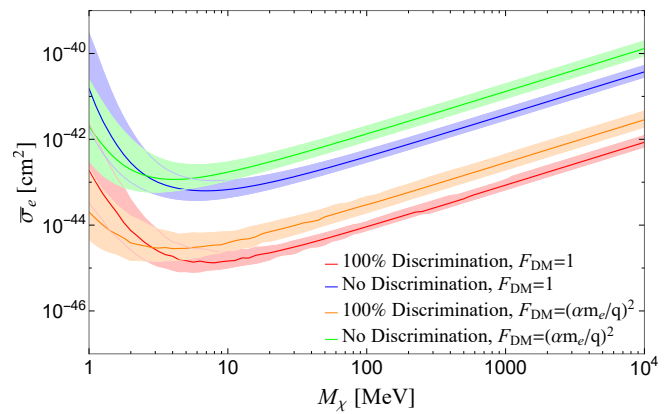


FIG. 9: 10^5 kg-yr “solid floor” discovery limits for χ -e scattering signal with no discrimination (blue/green curves) and 100% discrimination (red/orange curves) between electronic and nuclear scattering events. The blue/red curves correspond to $F_{DM} = 1$ and the green/orange curves correspond to $F_{DM} = (\alpha m_e/q)^2$. The light bands correspond to the pessimistic ($v_{earth} = 200$ km/s, $v_{escape} = 560$ km/s, $\rho_\chi = 0.35$ GeV/cm³) and optimistic ($v_{earth} = 280$ km/s, $v_{escape} = 640$ km/s, $\rho_\chi = 0.45$ GeV/cm³) scenarios of astrophysical uncertainties.

crystal can lower the ionization energy and probe lower values of M_χ [43]. The impact of the discovery limit for several doping techniques could be calculated in order to probe lower DM masses. Further, one could try to reduce the impact of the neutrino background by folding in annual modulation information for a long-exposure experiment and/or by employing detectors with directional recoil sensitivity [46].

Furthermore, in future work one could broaden the theoretical framework for DM at both the astrophysics and particle physics level. As we have demonstrated, the uncertainty in the velocity distribution, $f(\vec{v})$ has a significant impact on the discovery potential of a χ signal. Modeling of additional high-velocity contributions such as the Sagittarius stream, for example, will impact the DM spectrum and the annual modulation signal [40, 47] and would also play a role in distinguishing DM from the neutrino background. Moreover it would be natural to extend this work to the DM flux that has undergone “solar reflection” [48]. Second, while here we have focused on the impact of the neutrino background on DM discovery, it will also, in the event of a discovery, impact the ability of an experiment to determine uncertainties on the mass and cross section. The impact of astrophysical uncertainties on the mass and cross section determinations were considered for example in [49] in the context of DM-nuclear direct detection, and could be revisited in the light of DM-electron experiments. Lastly, to maximize the information gleaned from a future detection it would be useful to quantify how much data is required to extract particle physics information about DM interactions such as the nature of “dark form factors,” as has been done for DM-nuclear direct detection (e.g. [50, 51]).

Acknowledgments

We are grateful to Tien-Tien Yu for very helpful feedback regarding the QEdark package.

Note Added

While this paper was being completed the reference [52] appeared on the arXiv which addresses similar questions.

-
- [1] M. W. Goodman and E. Witten, *Detectability of Certain Dark Matter Candidates*, *Phys. Rev.* **D31** (1985) 3059.
- [2] SUPERCDMS collaboration, R. Agnese et al., *New Results from the Search for Low-Mass Weakly Interacting Massive Particles with the CDMS Low Ionization Threshold Experiment*, *Phys. Rev. Lett.* **116** (2016) 071301 [1509.02448].
- [3] DAMIC collaboration, A. Aguilar-Arevalo et al., *Search for low-mass WIMPs in a 0.6 kg day exposure of the DAMIC experiment at SNOLAB*, *Phys. Rev.* **D94** (2016) 082006 [1607.07410].
- [4] PANDAX-II collaboration, A. Tan et al., *Dark Matter Results from First 98.7 Days of Data from the PandaX-II Experiment*, *Phys. Rev. Lett.* **117** (2016) 121303 [1607.07400].
- [5] LUX collaboration, D. S. Akerib et al., *Results from a search for dark matter in the complete LUX exposure*, *Phys. Rev. Lett.* **118** (2017) 021303 [1608.07648].
- [6] S. Knapen, T. Lin and K. M. Zurek, *Light Dark Matter in Superfluid Helium: Detection with Multi-excitation Production*, *Phys. Rev.* **D95** (2017) 056019 [1611.06228].
- [7] XENON collaboration, E. Aprile et al., *First Dark Matter Search Results from the XENON1T Experiment*, *Phys. Rev. Lett.* **119** (2017) 181301 [1705.06655].
- [8] CRESST collaboration, G. Angloher et al., *Results on MeV-scale dark matter from a gram-scale cryogenic calorimeter operated above ground*, *Eur. Phys. J.* **C77** (2017) 637 [1707.06749].
- [9] Y. Hochberg, Y. Kahn, M. Lisanti, K. M. Zurek, A. G. Grushin, R. Ilan et al., *Detection of sub-MeV Dark Matter with Three-Dimensional Dirac Materials*, *Phys. Rev.* **D97** (2018) 015004 [1708.08929].
- [10] CRESST collaboration, F. Petricca et al., *First results on low-mass dark matter from the CRESST-III experiment*, in *15th International Conference on Topics in Astroparticle and Underground Physics (TAUP 2017) Sudbury, Ontario, Canada, July 24-28, 2017*, 2017, 1711.07692, <http://inspirehep.net/record/1637341/files/arXiv:1711.07692.pdf>.
- [11] CDEX collaboration, H. Jiang et al., *Limits on light WIMPs from the first 102.8 kg-days data of the CDEX-10 experiment*, 1802.09016.
- [12] W. Guo and D. N. McKinsey, *Concept for a dark matter detector using liquid helium-4*, *Phys. Rev.* **D87** (2013) 115001 [1302.0534].
- [13] Y. Hochberg, Y. Zhao and K. M. Zurek, *Superconducting Detectors for Superlight Dark Matter*, *Phys. Rev. Lett.* **116** (2016) 011301 [1504.07237].
- [14] Y. Hochberg, M. Pyle, Y. Zhao and K. M. Zurek, *Detecting Superlight Dark Matter with Fermi-Degenerate Materials*, *JHEP* **08** (2016) 057 [1512.04533].
- [15] G. Cavoto, E. N. M. Cirillo, F. Cocina, J. Ferretti and A. D. Polosa, *WIMP detection and slow ion dynamics in carbon nanotube arrays*, *Eur. Phys. J.* **C76** (2016) 349 [1602.03216].
- [16] Y. Hochberg, Y. Kahn, M. Lisanti, C. G. Tully and K. M. Zurek, *Directional detection of dark matter with two-dimensional targets*, *Phys. Lett.* **B772** (2017) 239 [1606.08849].
- [17] K. Schutz and K. M. Zurek, *Detectability of Light Dark Matter with Superfluid Helium*, *Phys. Rev. Lett.* **117** (2016) 121302 [1604.08206].
- [18] C. Kouvaris and J. Pradler, *Probing sub-GeV Dark Matter with conventional detectors*, *Phys. Rev. Lett.* **118** (2017) 031803 [1607.01789].
- [19] R. Budnik, O. Chesnovsky, O. Slone and T. Volansky, *Direct Detection of Light Dark Matter and Solar Neutrinos via Color Center Production in Crystals*, 1705.03016.
- [20] R. Essig, A. Manalaysay, J. Mardon, P. Sorensen and T. Volansky, *First Direct Detection Limits on sub-GeV Dark Matter from XENON10*, *Phys. Rev. Lett.* **109** (2012) 021301 [1206.2644].
- [21] R. Essig, M. Fernandez-Serra, J. Mardon, A. Soto, T. Volansky and T.-T. Yu, *Direct Detection of sub-GeV Dark Matter with Semiconductor Targets*, *JHEP* **05** (2016) 046 [1509.01598].
- [22] S. K. Lee, M. Lisanti, S. Mishra-Sharma and B. R. Safdi, *Modulation Effects in Dark Matter-Electron Scattering Experiments*, *Phys. Rev.* **D92** (2015) 083517 [1508.07361].
- [23] S. Derenzo, R. Essig, A. Massari, A. Soto and T.-T. Yu, *Direct Detection of sub-GeV Dark Matter with Scintillating Targets*, *Phys. Rev.* **D96** (2017) 016026 [1607.01009].
- [24] T. Emken, C. Kouvaris and I. M. Shoemaker, *Terrestrial Effects on Dark Matter-Electron Scattering Experiments*, *Phys. Rev.* **D96** (2017) 015018 [1702.07750].
- [25] R. Essig, T. Volansky and T.-T. Yu, *New Constraints and Prospects for sub-GeV Dark Matter Scattering off Electrons in Xenon*, *Phys. Rev.* **D96** (2017) 043017 [1703.00910].
- [26] DARKSIDE collaboration, P. Agnes et al., *Constraints on Sub-GeV Dark Matter-Electron Scattering from the DarkSide-50 Experiment*, 1802.06998.
- [27] B. W. Lee and S. Weinberg, *Cosmological Lower Bound on Heavy Neutrino Masses*, *Phys. Rev. Lett.* **39** (1977) 165.
- [28] B. Holdom, *Two $U(1)$'s and Epsilon Charge Shifts*, *Phys. Lett.* **166B** (1986) 196.
- [29] M. Pospelov, A. Ritz and M. B. Voloshin, *Secluded WIMP Dark Matter*, *Phys. Lett.* **B662** (2008) 53 [0711.4866].
- [30] J. McDonald, *Thermally generated gauge singlet scalars as*

- selfinteracting dark matter*, *Phys. Rev. Lett.* **88** (2002) 091304 [hep-ph/0106249].
- [31] L. J. Hall, K. Jedamzik, J. March-Russell and S. M. West, *Freeze-In Production of FIMP Dark Matter*, *JHEP* **03** (2010) 080 [0911.1120].
- [32] M. L. Graesser, I. M. Shoemaker and L. Vecchi, *Asymmetric WIMP dark matter*, *JHEP* **10** (2011) 110 [1103.2771].
- [33] T. Lin, H.-B. Yu and K. M. Zurek, *On Symmetric and Asymmetric Light Dark Matter*, *Phys. Rev.* **D85** (2012) 063503 [1111.0293].
- [34] A. Berlin and N. Blinov, *Thermal Dark Matter Below an MeV*, *Phys. Rev. Lett.* **120** (2018) 021801 [1706.07046].
- [35] J. Billard, L. Strigari and E. Figueroa-Feliciano, *Implication of neutrino backgrounds on the reach of next generation dark matter direct detection experiments*, *Phys. Rev.* **D89** (2014) 023524 [1307.5458].
- [36] F. Ruppin, J. Billard, E. Figueroa-Feliciano and L. Strigari, *Complementarity of dark matter detectors in light of the neutrino background*, *Phys. Rev.* **D90** (2014) 083510 [1408.3581].
- [37] J. B. Dent, B. Dutta, J. L. Newstead and L. E. Strigari, *Effective field theory treatment of the neutrino background in direct dark matter detection experiments*, *Phys. Rev.* **D93** (2016) 075018 [1602.05300].
- [38] P. F. Smith and J. D. Lewin, *Dark Matter Detection*, *Phys. Rept.* **187** (1990) 203.
- [39] G. Jungman, M. Kamionkowski and K. Griest, *Supersymmetric dark matter*, *Phys. Rept.* **267** (1996) 195 [hep-ph/9506380].
- [40] C. Savage, K. Freese and P. Gondolo, *Annual Modulation of Dark Matter in the Presence of Streams*, *Phys. Rev.* **D74** (2006) 043531 [astro-ph/0607121].
- [41] C. McCabe, *The Astrophysical Uncertainties Of Dark Matter Direct Detection Experiments*, *Phys. Rev.* **D82** (2010) 023530 [1005.0579].
- [42] R. Essig, J. Mardon and T. Volansky, *Direct Detection of Sub-GeV Dark Matter*, *Phys. Rev.* **D85** (2012) 076007 [1108.5383].
- [43] D. M. Mei, G. J. Wang, H. Mei, G. Yang, J. Liu, M. Wagner et al., *Direct Detection of MeV-Scale Dark Matter Utilizing Germanium Internal Amplification for the Charge Created by the Ionization of Impurities*, *Eur. Phys. J.* **C78** (2018) 187 [1708.06594].
- [44] B. J. Scholz, A. E. Chavarria, J. I. Collar, P. Privitera and A. E. Robinson, *Measurement of the low-energy quenching factor in germanium using an $^{88}\text{Y}/\text{Be}$ photoneutron source*, *Phys. Rev.* **D94** (2016) 122003 [1608.03588].
- [45] C. A. O'Hare, *Dark matter astrophysical uncertainties and the neutrino floor*, *Phys. Rev.* **D94** (2016) 063527 [1604.03858].
- [46] F. Kadribasic, N. Mirabolfathi, K. Nordlund, E. Holmström and F. Djurabekova, *Directional Sensitivity In Light-Mass Dark Matter Searches With Single-Electron Resolution Ionization Detectors*, *Phys. Rev. Lett.* **120** (2018) 111301 [1703.05371].
- [47] K. Freese, P. Gondolo, H. J. Newberg and M. Lewis, *The effects of the Sagittarius dwarf tidal stream on dark matter detectors*, *Phys. Rev. Lett.* **92** (2004) 111301 [astro-ph/0310334].
- [48] H. An, M. Pospelov, J. Pradler and A. Ritz, *Direct Detection of MeV-scale Dark Matter via Solar Reflection*, 1708.03642.
- [49] A. Friedland and I. M. Shoemaker, *Integrating In Dark Matter Astrophysics at Direct Detection Experiments*, *Phys. Lett.* **B724** (2013) 183 [1212.4139].
- [50] J. F. Cherry, M. T. Frandsen and I. M. Shoemaker, *Halo Independent Direct Detection of Momentum-Dependent Dark Matter*, *JCAP* **1410** (2014) 022 [1405.1420].
- [51] V. Gluscevic, M. I. Gresham, S. D. McDermott, A. H. G. Peter and K. M. Zurek, *Identifying the Theory of Dark Matter with Direct Detection*, *JCAP* **1512** (2015) 057 [1506.04454].
- [52] R. Essig, M. Sholapurkar and T.-T. Yu, *Solar Neutrinos as a Signal and Background in Direct-Detection Experiments Searching for Sub-GeV Dark Matter With Electron Recoils*, 1801.10159.